Observation of unoccupied states of SnTe(111) using pump-probe ARPES measurement

Hiroshi Ito,[1] Yusuke Otaki,[1] Yuta Tomohiro,[1] Yukiaki Ishida,[2,*] Ryota Akiyama,[3] Akio Kimura,[4,5] Shik Shin,[2] and Shinji Kuroda[1,†]

[1]*Institute of Materials Science, University of Tsukuba, 1-1-1 Tennoudai, Tsukuba, Ibaraki 305-8573, Japan*
[2]*Institute for Solid State Physics, The University of Tokyo, 5-1-5 Kashiwa-no-ha, Kashiwa, Chiba 277-8581, Japan*
[3]*Department of Physics, The University of Tokyo, 7-3-1 Hongo, Bunkyo, Tokyo 113-0033, Japan*
[4]*Department of Physical Sciences, Graduate School of Science, Hiroshima University, 1-3-1 Kagamiyama, Higashi-Hiroshima, Hiroshima 739-8526, Japan*
[5]*Graduate School of Advanced Science and Engineering, Hiroshima University, 1-3-1 Kagamiyama, Higashi-Hiroshima, Hiroshima 739-8526, Japan*

(Received 6 January 2020; accepted 15 September 2020; published 22 October 2020; corrected 9 November 2020)

A IV-VI compound SnTe is proposed to be a topological crystalline insulator (TCI), and the band structures have been studied by using angle-resolved photoemission spectroscopy (ARPES). However, the topological surface states (TSSs) that hallmark the nontrivial topology disperse mostly in the unoccupied side where access via ARPES is limited. Here we investigate the (111) face of a SnTe film by using pump-probe ARPES. We find distinct energy sections in the unoccupied side that behave differently in terms of the excitation and recovery dynamics. From these different behaviors, the boundaries of these sections are attributed to the edges of the conduction and valence bands. High statistics data reveal that the TSSs are traversing the band gap, which evidences that SnTe belongs to a TCI. We also find that the bulk bands near the gap show splitting, which is attributed to the Rashba effect occurring in the dipolar surface region.

DOI: 10.1103/PhysRevResearch.2.043120

I. INTRODUCTION

A topological crystalline insulator (TCI) has been introduced as a new class of insulators [1]. The nontrivial topology of the bulk band structure is protected by point group symmetries of the crystal [1,2], instead of the time-reversal symmetry in Z_2 topological insulators. As a result of the nontrivial topology, massless spin-polarized modes emerge on the surfaces of TCI. The topological surface states (TSSs) serve as a hallmark of TCI, providing a platform for realizing different spintronic functionalities.

Being categorized as narrow-gap semiconductors, SnTe and other IV-VI compounds have long been studied for application of optical devices in the midinfrared range [3,4]. SnTe has also attracted much attention in its ferroelectric properties, because the nonpolar (centrosymmetric) rocksalt (RS) structure of the IV-VI compounds is inherently soft, or vulnerable to change into a polar (noncentrosymmetric) rhombohedral structure [5]: In the SnTe case, the structural transition was reported in bulk crystals below ∼100 K depending on the hole concentration [6,7]. After the foundation of the TCI class [1,2], SnTe has gained renewed interest as its exemplary: The nontrivial topology of SnTe is protected with respect to the mirror reflection symmetry about the six {110} planes of the RS structure [2]. In the pursuit to reveal the characteristics features of TCIs, SnTe and their siblings, such as (Pb,Sn)Te and (Pb,Sn)Se, have been investigated by angle-resolved photoemission spectroscopy (ARPES) [8–15] as well as by electrical transport [16–19] and optical measurements [20,21]. Another interest that has recently been arising in IV-VI compounds is the discovery of giant Rashba splitting in the valence band of GeTe, and the relation to the polar structure and field effects near the surface was discussed [22,23].

In reality, the SnTe crystals are not insulating because the bulk crystals contain a high concentration of Sn vacancies that act as acceptors. As a result, the Fermi level (E_F) is located within the valence band (VB), with the band gap ranging in the unoccupied side, or energies at $E > E_F$. Because ARPES is not suited to track the dispersions above E_F, the electronic states around and across the bulk band gap have remained elusive. In fact, ARPES studies to date on SnTe [8,10–13] claimed the detection of the TSSs by observing only the tails of their dispersions. The tails were assigned to the surface states because their dispersions along the direction normal to the surface were estimated to be small [8,13] from almost no variation with the excitation energy.

In time-resolved ARPES (TARPES) implemented by the pump-probe method, a pump pulse hits the sample, and subsequently a probe pulse snapshots the nonequilibrated state induced by the pump. The snapshot can be taken when the redistributed electrons are transiently filling the unoccupied states; TARPES has the capability to visualize the bands in

*ishiday@issp.u-tokyo.ac.jp
†kuroda@ims.tsukuba.ac.jp

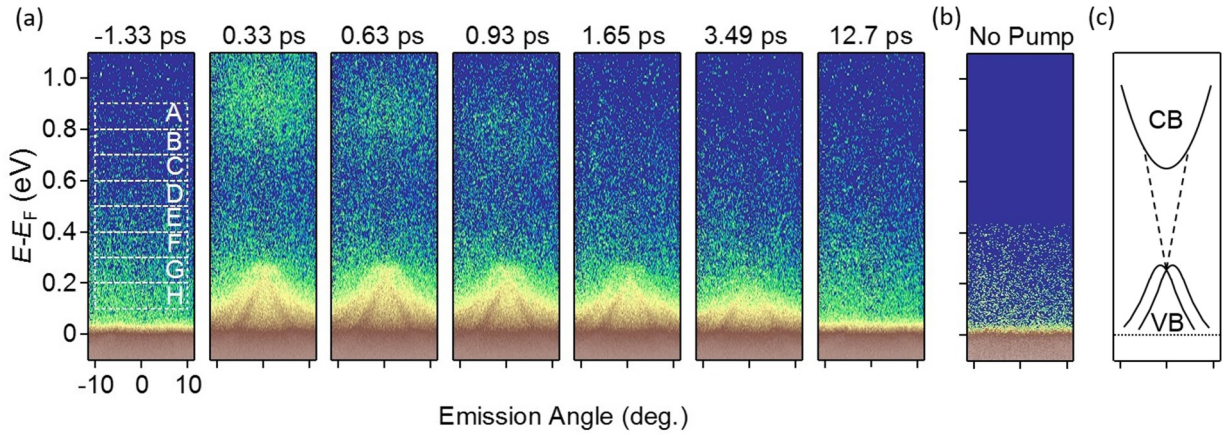

FIG. 1. (a) Snap-shot ARPES images around $\bar{\Gamma}$ point of the SnTe (111) surface recorded at various delay time t in the range of $t = -1.33$–12.7 ps. The horizontal axis corresponds the emission angle along the direction $\bar{\Gamma}$ to $\bar{\mathrm{M}}$. The frames A–H shown in the panel recorded at $t = -1.33$ ps are set as follows: The widths in energy and angle are 0.1 eV and 20°, respectively; the frames A, B, …. H are centered, respectively, at 0.85, 0.75, …, and 0.15 eV in energy, and at 0° in the emission angle. (b) The ARPES image without the irradiation of a pump pulse. The data (a), (b) were both obtained by the measurement at around 25 K. (c) Sketch of the band dispersion of bulk CB, VB, and the surface state, which we deduce from the time-resolved ARPES images in (a) and also from the time-integrated image in Fig. 3.

the unoccupied side [24,25]. Besides, the existence of the near-surface field, or surface band bending, can be inferred through investigating the surface photovoltage (SPV) effect [26–29]. Here, we investigate the electronic structures of SnTe by using TARPES; the measurement is done at temperatures ranging from 25 to 300 K, which covers a critical temperature of the possible structural transition below 100 K [6,7]. To this end, we fabricated a single-crystalline SnTe thin film with the [111] direction normal to the surface. In contrast to (001), the (111) surface can host the TSSs forming a Dirac cone centered at $\bar{\Gamma}$, or around the normal emission $\theta = 0^\circ$ in the ARPES image. The appearance of the cone around $\bar{\Gamma}$ makes it possible for the cone to be detected by our 1.5-eV pump and 5.9-eV probe TARPES apparatus [30].

II. EXPERIMENTAL METHODS

We grew a SnTe (111) thin film by molecular beam epitaxy (MBE) on a CdTe template [31], a thick CdTe layer deposited on a GaAs wafer. In order to ensure the surface flatness, which is critical for the ARPES measurement, we grew a SnTe layer as thick as 1 μm. The grown SnTe film was transferred to the facility of TARPES measurement without being exposed to air using a homemade portable vacuum chamber. The crystal structure of the grown film was *ex situ* examined by the x-ray diffraction (XRD) measurements. The out-of-plane and in-plane XRD scans revealed that the SnTe layer is distorted to the rhombohedra structure, but the magnitude of the distortion is too small to induce the ferroelectric transition and the topological nature of SnTe is considered to be practically preserved. (See Appendix A for details of the growth and characterizations of the sample.) The TAPRES measurement was performed with 1.5-eV pump and 5.9-eV probe pulses of the duration of 170 fs, which were derived from a Ti-sapphire laser system operating at a repetition rate of 250 Hz [30]. In the measurement, the energy resolution of less than 20 meV and the time resolution of 240 fs were attained [30].

III. EXPERIMENTAL RESULTS

We first present the result of TARPES measurement done with the intensity of a 1.5-eV pump pulse of 325 μJ/cm^2 at a low temperature around 25 K. Figure 1(a) shows TARPES images recorded when the delay time t was varied from -1.33 to 12.7 ps. The image recorded before the arrival of the pump pulse ($t = -1.33$ ps) represents the electron distribution in equilibrium; Therein, virtually no signal appears at energies above E_F. At $t = 0$ ps, the pump pulse arrives, and signal emerges at $E > E_F$ because the unoccupied state is filled by the carriers excited by the pump. The recovery to the equilibrium state succeeds, and the distribution at $t = 12.7$ ps is mostly settled back to the equilibrium distribution. See also Supplemental Material [32].

We checked that the TARPES image recorded at $t = -1.33$ ps showed no discernible difference from that recorded without pump, namely, from the ordinary ARPES image; see Fig. 1(b). The TARPES image recorded just before the arrival of the pump is thus confirmed to represent the equilibrium distribution. In other words, the effect due to the previous pump pulse was negligible at the arrival of the next pulse in the repetitive pumping at an interval of 4 μs. If the effect of the previous pulse survives, it should include pump-induced heating and SPV effects. The latter can be induced when the band bending develops around the surface region in an electrically insulating sample. The absence of SPV in the present measurement is reasonable because the surface band bending cannot be expected in our sample with a high hole concentration of 3×10^{20} cm^{-3}.

In some of the TARPES images shown in Fig. 1(a), one can see the VB dispersing up to E–$E_\mathrm{F} \sim 0.3$ eV. The dispersion is not a simple parabola, but shows some splitting, which can be ascribed to the Rashba effect as we shall discuss later. Weak signals can also be seen at E–$E_\mathrm{F} > \sim 0.6$ eV; and additionally, still weaker signals may also be discerned at 0.3–0.6 eV above E_F. The former is attributed to the bulk conduction band (CB), and the latter, to the TSSs that traverse the band gap. The

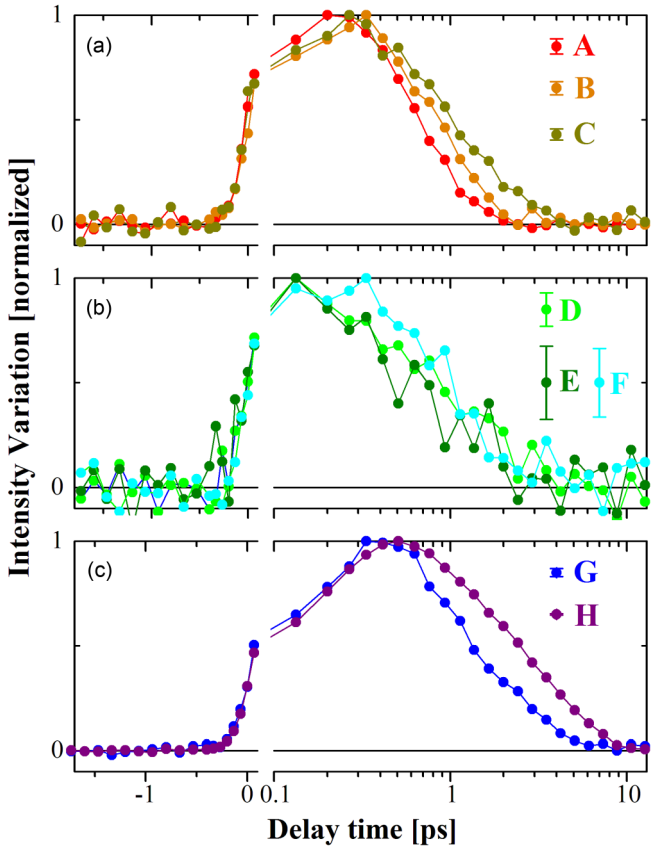

FIG. 2. Carrier dynamics in the respective electronic states. Temporal evolution of the PE intensity in the energy frames (a) A–C, (b) D–F, and (c) G,H, denoted in the snapshot ARPES image at $t = -1.33$ ps in Fig. 1. The PE intensity is normalized by the peak value for the respective curves. The magnitude of error bars for the respective curves is indicated in the legend.

existence as well as the assignment of these states will be solidified later.

The analysis into the energy dependence of the excitation and recovery dynamics helps us to nail down the assignment as well as the existence of the bands. In order to see the energy dependence in these carrier dynamics, we set frames A–H that cover the energy region from 0.9 to 0.1 eV, as represented in the panel for $t = -1.33$ ps and the caption of Fig. 1(a). Then, we evaluate the temporal variation of the signal intensity in each frame. The variations normalized to the peak height are plotted in Fig. 2. The curves for the frames A to H represent the change in number of the carriers in the regions from high (A) to low (H) energies.

First of all, it should be noted that the variations of the signal intensity are detected in all the frames spanning from 0.1 to 0.9 eV; the photoemission (PE) intensity rises upon the excitation of carriers into the unoccupied states and then decays, the carrier distribution recovering to the equilibrium distribution. Similar temporal variations in all the frames confirm that the electronic states, which accommodate electrons, exist throughout the whole energy region including E–$E_F >$ 0.3 eV. Second, the energy region can be separated into three sections regarding the rise and recovery profiles as follows: (1) In the first section [0.9, 0.6 eV] (frames A–C), the intensity rises quickly upon the excitation and reaches the maximum at $t = 0.2-0.4$ ps, while the recovery slows as the energy is lowered. (2) In the second section [0.6, 0.3 eV] (D–F), it would be difficult to discern differences in the decay profile from those in the first and third sections, due to scattered profiles with low signal intensities. But it looks like the rise time becomes shorter compared to the first section. (3) In the final section at E–$E_F < 0.3$ eV (G,H), where the VB is located, the rise of the intensity is delayed clearly compared to the first and second sections; it reaches the maximum at around $t = 0.5$ ps. And the recovery slows again as the energy is lowered. The boundary between the second and third sections at E–$E_F \sim 0.3$ eV is readily assigned to the VB maximum. On the other hand, the rise of the intensity exhibits different behaviors between the first and second sections though the recovery profiles do not exhibit distinct features. In addition, taking into account the shape of the band dispersion, which becomes clearly visible in the time-integrated ARPES images (shown later), the first section at E–$E_F >$ ~0.6 eV could be assigned to the CB, with the bottom of the CB located in frame C [0.7, 0.6 eV]. In the CB, the recovery to the equilibrium becomes slower as approaching the CB minimum because the carriers are temporarily accumulated at the bottom of the CB and then flow into the lower-energy states. On the other hand, in the VB, both the rise and recovery of the intensity become slower as the energy is lowered and approaches the E_F. This would reflect a delay in filling the states due to the flow of carriers from the higher-energy states. The first and third sections are thus assigned to the bulk CB and VB, and the second section in between to the bulk band gap, its energy width being roughly corresponding to the reported value ~0.3 eV for the band gap of SnTe. Then we are led to attribute the states existing in the second section to the TSSs traversing the bulk band gap.

In order to obtain a clear image of the weak trace above the VB, we acquired another TARPES dataset composed of 21 snapshots taken in the time domain of [0, 0.76 ps], and added up all the snapshots. In the time-integrated image shown in Fig. 3(a), the VB and CB can be seen more clearly than in the time-resolved images shown in Fig. 1. One can see the splitting of the VB top more clearly. In addition, a V-shaped trace can be discerned in the second section [0.6, 0.3 eV]. Figure 3(b) shows the momentum distribution curves (MDCs) of the integrated image. The V-shaped dispersion can be tracked by the peaks in the MDCs: A broad peak seen in the MDC for the top of the VB is split into two peaks and the separation becomes wider as the energy is increased and finally the two peaks merge into the bottom of CB, which also looks like it is split into two bottoms. It is reasonable to assign the observed V-shaped dispersion to the TSSs that traverse the band gap. Certainly one might not be able to exclude entirely the possibility of the incoherent spectral weight for the observed spectra within the band gap, but such an effect, typically observed in strongly correlated system [33], would not be likely in the present case. The band dispersion looks as though it is almost linear, as traced by dotted lines in the figures, though the exact shape might be hard to be determined due to signal fluctuations. The crossing point of this dispersion, or the Dirac point (DP) of the TSSs is located at ~0.2 eV, which is below the top of the VB. The locus of the DP is not consistent with

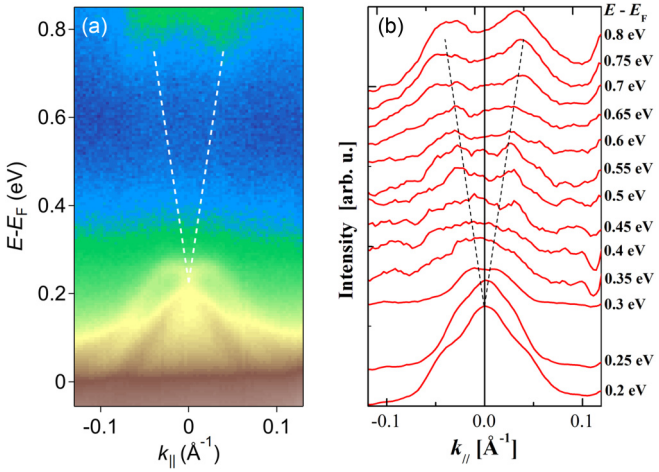

FIG. 3. (a) Time-integrated ARPES image around $\bar{\Gamma}$ point, obtained by integrating time-resolved snapshot images in the range of $t = 0$–0.76 ps. This image was deduced from the result of another set of measurement using probe pulses of a higher intensity than that shown in Figs. 1, 2, but at the same temperature around 25 K. (b) Momentum distribution curves (MDCs) at the respective energy ranges deduced from the time-integrated ARPES image in (a).

that reported previously based on the conventional ARPES measurements [11,15].

The data presented so far were those recorded around 25 K. To get insights into the effect of a possible structural transition, which was reported to take place below 100 K in bulk crystals [6,7], on the bulk band dispersion, we also performed measurements above 100 K. Figure 4 shows the TARPES images recorded at 110, 150, and 300 K. The pump-probe delay and fluence were set to 0.27 ps and 325 mJ/cm^2, respectively. Although the band dispersion seen in the images becomes blurred at elevated temperatures, the splitting of the VB is retained even at 300 K. These results suggest that the splitting in the VB does not originate from the structural transition of the crystal in bulk.

IV. DISCUSSION

The surface band observed in our TARPES measurement exhibits a Dirac-cone shape, but the positon of the DP is different from those reported previously [11,15]; The conventional

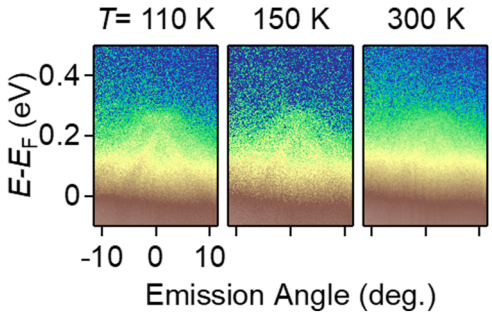

FIG. 4. Time-resolved ARPES images at a fixed delay time $t = 0.27$ ps measured at elevated temperatures of 110, 150, and 300 K, respectively.

ARPES studies on the SnTe (111) surface of bulk crystals and thin films reported that the position of DP was estimated at 80 meV [11] and 0.65 eV [15] above E_F, respectively. However, in these studies, the DP was not directly observed and its position was only deduced from the extrapolation of the observed lower-branch of the Dirac cone, overlapping with the bulk VB. On the other hand, a Dirac cone of similar shape to our result, that is, the V-shaped linear dispersion and the DP below the top of VB, was observed on the (111) surface of a mixed crystal $Pb_{0.54}Sn_{0.46}Te$ on the topological side [14]. According to theoretical calculations, the shape of the Dirac cone on the SnTe (111) surface depends on the surface termination; the DP lies close to the top of VB for the Sn-terminated surface, while it lies close to the bottom of CB for the Te-terminated surface [34,35]. Our result looks rather close to the theoretical prediction for the Sn-terminated surface, although the surface termination has not been examined in the present study.

Overall, the relaxation of carriers excited to the bulk CB and the surface band turned out to be fast; as shown in Fig. 2, the temporal variations of the PE intensity exhibit rapid decays within a few ps, though there are slight variations with the energy range. In particular, any apparent bottleneck effect [36] was not observed in the carrier relaxation in the surface band. This may be related to the position of the DP, which overlaps with the bulk VB. The carrier relaxation reported in conventional TI materials shows wide variations depending on the conductive properties of crystals, exemplified by fast relaxation of the order of few ps in bulk-conductive Sb_2Te_3 [36] and slow relaxation of ~400 ps in bulk-insulating $(Bi_{0.43}Sb_{0.56})_3Te_3$ [29]. The slow relaxation in the latter case was attributed to the position of Fermi level close to the DP [29]. The fast relaxation in the present study would be consistent with the position of E_F away from the DP in the degenerate electronic state of SnTe in an actual crystal.

In the time-resolved and time-integrated ARPES images in Figs. 1 and 3, the bulk VB exhibits a large splitting, which is ascribed to the Rashba effect. So far, the Rashba splitting of the bulk VB has not been reported in SnTe. This might be just because the top of the VB has not been accessible in the conventional ARPES measurement. Instead, in a mixed crystal $Pb_{0.54}Sn_{0.46}Te$, the Rashba splitting of the bulk VB was revealed by conventional ARPES measurement [14]; in that study, the top of the VB became accessible in the measurement on an n-type crystal doped with Bi as a donor impurity. The splitting of the VB in SnTe observed here shows a close resemblance to that observed in $Pb_{0.54}Sn_{0.46}Te$; the magnitude of splitting is similar and the surface band converges around the crossing point of the split VB. From the momentum splitting $2\Delta k_R$ and the energy shift E_R estimated in the time-integrated ARPES image in Fig. 3, we derive the Rashba constant $\alpha_R = 2E_R/\Delta k_R$. The value derived $\alpha_R \sim 3.6$ eV Å is almost identical to the maximal value 3.8 eV Å in Bi-doped $Pb_{0.54}Sn_{0.46}Te$ [14], and also comparable to the values of $\alpha_R = 2$–4 eV Å reported for typical materials of giant Rashba effect, such as BiTeI [37] or α-GeTe [22,23]. The giant Rashba splitting in these materials originates from the breaking of space-inversion symmetry in noncentrosymmetric crystal structures. In the case of SnTe, the previous

studies on bulk crystals reported the phase transition from RS to rhombohedral (noncentrosymmetric) structure below 100 K [6,7]. However, in the thin film studied here, it is not likely that the phase transition of bulk structure causes the observed Rashba splitting in the VB, as discussed below. First, the XRD analysis at room temperature revealed that the SnTe layer is slightly distorted with the elongation along ⟨111⟩ direction (see Appendix A for details), presumably due to a small lattice mismatch with the CdTe underlayer, but the magnitude of distortion is estimated far too small to explain the observed splitting [38]. The phase transition at a low temperature is also unlikely in the temperature range studied here, since we did not observe any critical behavior in the temperature dependence of electrical resistance [19]. This is a different case from the previous studies on bulk crystals, reporting an anomalous increase of resistance in the vicinity of the transition temperature [7], due to an enhancement of carrier scattering by soft TO phonons [6]. In addition, we observed the Rashba splitting at the top of VB at higher temperatures up to 300 K. From these experimental results, the observed large splitting of VB could not be attributed to the breaking of the inversion symmetry of the bulk structure.

In Ref. [14], reporting similar splitting in the VB in a mixed crystal $Pb_{0.54}Sn_{0.46}Te$ in the conventional ARPES measurement, the authors attributed the observed splitting to the so-called surface band bending; they argued that the inversion symmetry is broken near the surface region, induced by an electric field normal to the surface due to the formation of a depletion layer and that the band bending near the surface region, which was caused by the pinning of the Fermi level at the surface, was enhanced by the charge accumulation in Bi-doped crystals [39]. However, it is not clear whether such a large splitting as observed in the present case can be expected at a potential gradient of the order of 1 V/nm. In addition, if the band bending is induced by the pinning of the Fermi level at the surface state, it should be affected by photoexcited carriers; high-density carriers excited by an intense pump pulse should contribute to relax the band bending [29]. But in our TARPES measurement, no SPV effect was discerned (see Fig. 9 in Appendix A), which denies the existence of a significant band bending, as an origin of the Rashba splitting. Alternatively, so-called surface Rashba effect could be considered as a possible origin of the observed splitting; a large Rashba splitting arises at the surface of a solid composed of a heavy element, as discovered on the Au(111) surface [40], due to an asymmetric form of the wave function along the direction normal to the surface (space-inversion symmetry breaking) [41]. For the surface Rashba splitting, the magnitude of splitting should be determined by the potential gradient defined for the real wave function, which has a significant component near the core due to Coulomb potential of the nuclei. As a result, the surface Rashba splitting is expected to be large on the surface of heavy elements, though it would not be clear whether this surface Rashba effect is also applicable to our case of the SnTe(111) surface. In addition, this surface Rashba effect, which is not likely to be affected by the irradiation of light, may possibly be responsible for the observed splitting on the SnTe(111) surface. It is expected that this surface Rashba effect would be sensitive to the atomic arrangement on the surface. According to theoretical studies, the splitting of the valence band similar to that observed in the present case was reproduced for a reconstructed [42] or pristine [43] surface. In the present study, the surface reconstruction was not apparently detected in the low-energy electron diffraction (LEED) observation prior to the ARPES measurement, but detailed analyses on the surface state would be needed to understand the origin of the splitting of the bulk band.

V. CONCLUSION

In summary, we have performed TARPES measurement on the (111) surface of a SnTe thin film grown by MBE. We observed the whole structure of the surface band, having the Dirac point below the top of the bulk VB. This result is much different from that extrapolated from the observation of the lower part of the surface band by the conventional ARPES measurement. In the pump-and-probe measurement with the variation of delay time, we revealed a fast relaxation of carriers excited to the bulk CB and the surface band on the order of a few ps. We also revealed that the bulk VB exhibits a large splitting due to the Rashba effect. These experimental findings demonstrate the potential of this material for application in spintronics by using spin-polarized states both in the TSS and Rashba-split bulk bands.

ACKNOWLEDGMENTS

The authors thank T. Koyano in the Cryogenic Division of Research Facility Center for Science and Technology, University of Tsukuba for electrical measurements using PPMS and T. Suemasu for XRD measurements. The TARPES measurement was performed by the joint research of ISSP, the University of Tokyo. This study has partially been supported by JSPS KAKENHI Grants No. 16H00983, No. 17K18749, No. 18H01148, and No. 18H01857. S.K. acknowledges the support from the Center for Spintronics Research Network (CSRN), Osaka University, Japan.

APPENDIX A: SAMPLE GROWTH AND CHARACTERIZATION

We grew a SnTe (111) thin film using an MBE chamber equipped with a compound source of SnTe. As a substrate, we used a conductive CdTe template [31], in which a thick layer of CdTe doped with nitrogen (N) was deposited on a conductive GaAs (111)A wafer. During the growth of SnTe, we kept the substrate temperature at 250 °C, an optimal value for the epitaxial growth of SnTe. In order to ensure the surface flatness, we grew a relatively thick SnTe layer of a thickness around 1 μm. We checked the surface morphology by *in situ* observation using reflection high-energy electron diffraction (RHEED). Figure 5 shows RHEED images before (a) and during (b) and (c) the growth of the SnTe layer. During the growth of SnTe, we observed a (1 × 1) streak pattern without surface reconstruction, which indicates the two-dimensional growth of a single-crystalline SnTe layer of a good structural quality. After the growth of SnTe, we transferred the grown film into a homemade portable vacuum chamber without

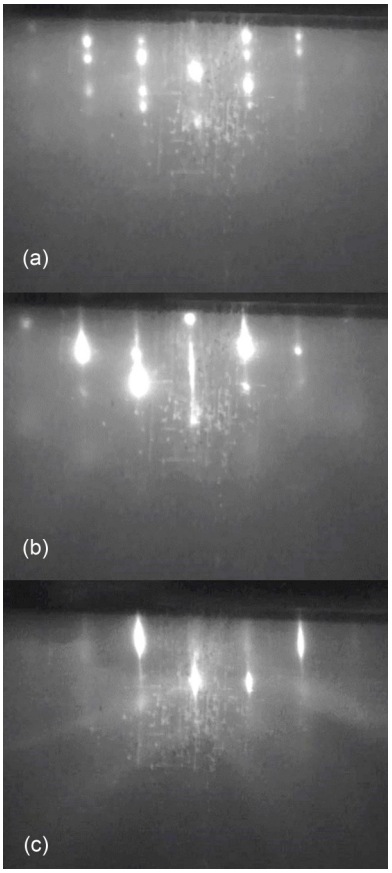

FIG. 5. RHEED images before and during the growth of a SnTe layer; (a) before the growth of SnTe (the surface of the CdTe template), (b) 5 min after starting the growth of SnTe, (c) 7 h after starting the growth, when the thickness of the SnTe layer reached around 1 μm.

being exposed to air and transported it to the facility of TARPES measurement at ISSP, University of Tokyo with keeping the vacuum of the order of 10^{-7}Torr. In the preparation chamber of the ARPES facility, we cleaned the SnTe surface by heating the sample up to around 200 °C. Figure 6 shows the LEED image after the heating. We observed the fundamental diffraction spots up to the second-order without any reconstruction, suggesting a clean surface of the SnTe layer.

We performed *ex situ* structural characterizations using atomic-force microscopy (AFM) and XRD at room temperature. Figure 7 shows an AFM image of the SnTe surface. Though the surface of the SnTe layer grown on CdTe exhibits multidomain structure [31], it is almost flat with a root mean square of height around 0.3 nm within the terrace region. Figure 8 shows the result of out-of-plane and in-plane XRD scans of the grown film. In the out-of-plane $2\theta/\omega$ scan profiles shown in Fig. 8(a), we observed the diffractions only from the SnTe (111) plane and those of CdTe and GaAs, without detection of those from any extrinsic phase nor from different orientations of SnTe. From the diffraction angles in the out-of-plane and in-plane scans shown in Figs. 8(b) and 8(c), the out-of-plane and in-plane lattice constants are derived as $a_\perp = 6.335$ Å and $a_\parallel = 6.327$ Å, respectively. A slight difference between these two values indicates that the SnTe layer is strained due to a small lattice mismatch with the CdTe underlayer. The cube of the RS structure is elongated along the $\langle 111 \rangle$ direction, equivalent to a rhombohedral distortion. From the values of $a_\perp$ and $a_\parallel$, the corner angle of unit cell of rhombohedron is derived as $a \sim 89.95^\circ$. Theoretically, it was predicted that the ferroelectric transition of SnTe from cubic to rhombohedral structure induces the transition to "ferroelectric Rashba semiconductor" [38], but the lattice distortion in the present case is much smaller and would not impact the band structure.

FIG. 6. LEED image of the SnTe layer after the thermal annealing.

For the characterization of electrical properties, we grew another SnTe thin film by MBE with the same growth condition on an insulating CdTe template; a thick CdTe layer without N doping on a semi-insulating GaAs (111)A wafer. We performed the resistivity and Hall measurement on this SnTe thin film and obtained a hole concentration of

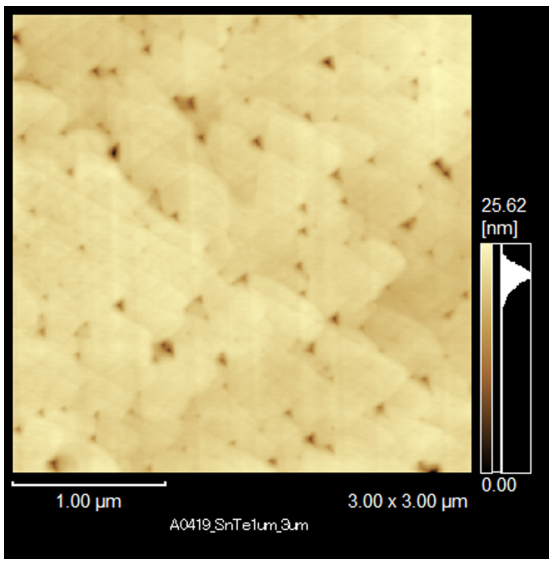

FIG. 7. AFM image of the surface of the 1-μm-thick SnTe layer grown on a CdTe template. The scanned range is $3 \times 3\,\mu\text{m}^2$.

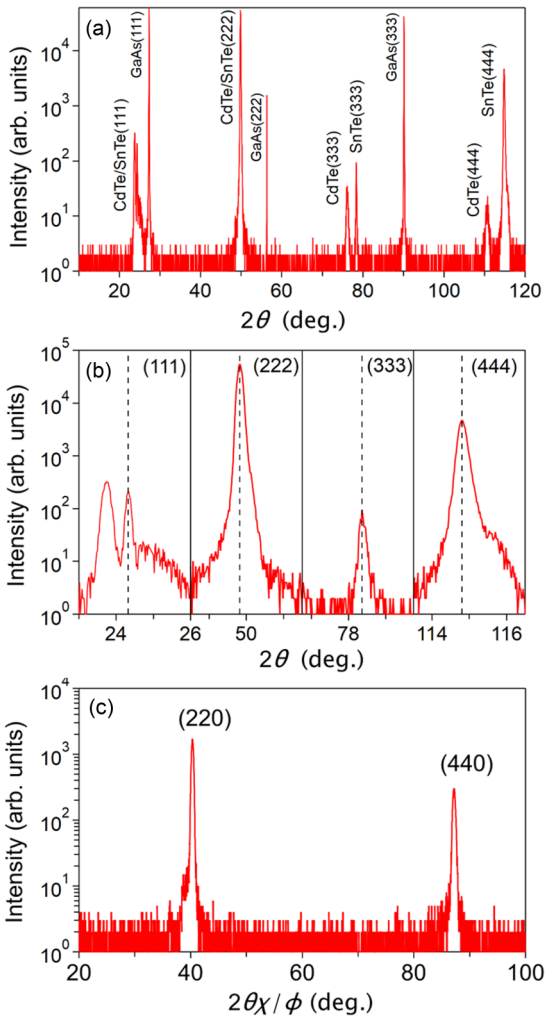

FIG. 8. The out-of-plane and in-plane XRD scan profiles of the grown film. (a) The profile of the out-of-plane $2\theta/\omega$ scan in the entire range of diffraction angle. (b) The diffraction of SnTe (*nnn*) planes in an enlarged scale of diffraction angle [the same scan as shown in (a)]. (c) The diffraction of SnTe (*nn*0) planes in the in-plane $2\theta\chi/\phi$ scan.

3×10^{20} cm^{-3} and mobility around 3500 cm^2/Vs at room temperature.

APPENDIX B: TIME-RESOLVED ARPES MEASUREMENT AND SURFACE PHOTOVOLTAGE (SPV) EFFECT

TARPES measurement was performed by exciting the sample using pump and probe pulses of 1.48 and 5.98 eV, which were delivered from the Ti:sapphire laser system operating at a repetition rate of 250 kHz [30]. The emitted photoelectron was analyzed using a hemispherical electron analyzer with an energy resolution of ∼15 meV [30]. The spot diameters of pump and probe pulses were 280 and 85 μm, respectively.

Figure 9 shows the angle-integrated energy distribution curves (EDC) derived from the time-resolved ARPES images

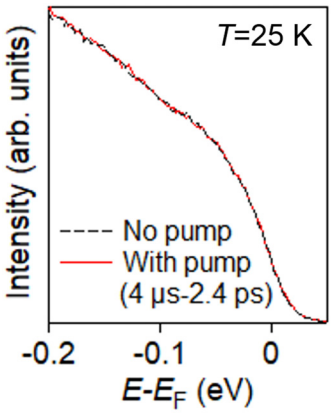

FIG. 9. Angle-integrated EDC derived from the time-resolved ARPES images without and with a pump pulse. A black dashed curve is derived from the ARPES image without pump and a red solid curve is derived from that prior to a pump pulse ($t = -2.4$ ps).

without and with a pump pulse. The two curves representing the results without and with a pump pulse almost overlap each other, suggesting that a pump-induced potential shift due to the SPV effect is negligible.

APPENDIX C: VALENCE BAND STRUCTURE IN THE OCCUPIED SIDE

Figure 10 shows a "normalized" ARPES image, derived from the time-integrated ARPES image shown in Fig. 3(a).

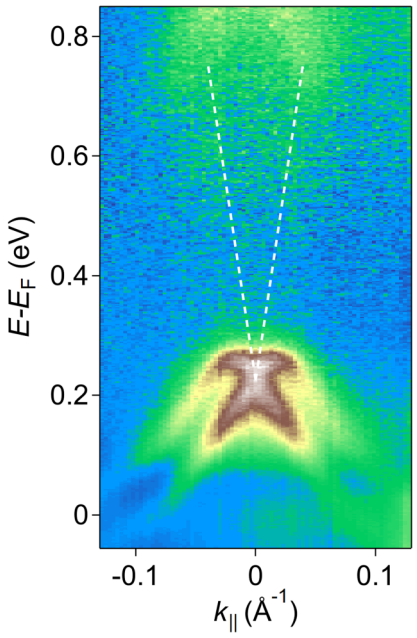

FIG. 10. "Normalized" ARPES image, derived from the time-integrated ARPES image shown in Fig. 3(a). Here we normalized the signal intensities at the respective energies, in order to see clearly variations of intensity at the respective energies.

Here we normalized the signal intensities at the respective energies, in order to see clearly variations of intensity at the respective energies. As shown in this image, one can discern one of the split states of the valence band even in the occupied side $E - E_F < 0$, which continues from the band structure in the occupied side across the Fermi level.

[1] L. Fu, Topological Crystalline Insulators, Phys. Rev. Lett. **106**, 106802 (2011).

[2] T. H. Hsieh, H. Lin, J. Liu, W. Duan, A. Bansil, and L. Fu, Topological crystalline insulators in the SnTe material class, Nat. Commun. **3**, 982 (2012).

[3] H. Holloway and J. N. Walpore, MBE techniques for IV-VI optoelectronic devices, Prog. Cryst. Growth Charact. **2**, 49 (1979).

[4] H. Preier, Recent advances in lead-chalcogenide diode lasers, Appl. Phys. **20**, 189 (1979).

[5] X. Zhang, Q. Liu, J.-W. Luo, A. J. Freeman, and A. Zunger, Hidden spin polarization in inversion-symmetric bulk crystals, Nat. Phys. **10**, 387 (2014).

[6] M. Iizumi, Y. Hamaguchi, K. F. Komatsubara, and Y. Kato, Phase transition in SnTe with low carrier concentration, J. Phys. Soc. Jpn. **38**, 443 (1975).

[7] K. L. I. Kobayashi, Y. Kato, Y. Katayama, and K. F. Komatsubara, Carrier-Concentration-Dependent Phase Transition in SnTe, Phys. Rev. Lett. **37**, 772 (1976).

[8] Y. Tanaka, Z. Ren, T. Sato, K. Nakayama, S. Souma, T. Takahashi, K. Segawa, and Y. Ando, Experimental realization of a topological crystalline insulator in SnTe, Nat. Phys. **8**, 800 (2012).

[9] P. Dziawa *et al.*, Topological crystalline insulator states in$Pb_{1-x}Sn_xSe$, Nat. Mater. **11**, 1023 (2012).

[10] S. Y. Xu *et al.*, Observation of a topological crystalline insulator phase and topological phase transition in $Pb_{1-x}Sn_xTe$, Nat. Commun. **3**, 1192 (2012).

[11] Y. Tanaka, T. Shoman, K. Nakayama, S. Souma, T. Sato, T. Takahashi, M. Novak, K. Segawa, and Y. Ando, Two types of dirac-cone surface states on the (111) surface of the topological crystalline insulator SnTe, Phys. Rev. B **88**, 235126 (2013).

[12] C.-H. Yan *et al.*, Growth of topological crystalline insulator SnTe thin films on Si(111) substrate by molecular beam epitaxy, Surf. Sci. **621**, 104 (2014).

[13] C. Yan *et al.*, Experimental Observation of Dirac-Like Surface States and Topological Phase Transition in $Pb_{1-x}Sn_xTe(111)$ Films, Phys. Rev. Lett. **112**, 186801 (2014).

[14] V. V. Volobuev *et al.*, Giant Rashba splitting in $Pb_{1-x}Sn_xTe(111)$ topological crystalline insulator films controlled by Bi-doping in the bulk, Adv. Mater. **29**, 1604185 (2017).

[15] Yi. Zhang *et al.*, ARPES study of the epitaxial grown topological crystalline insulator SnTe(111), J. Electron Spectrosc. Relat. Phenom. **219**, 35 (2017).

[16] M. Safdar, Q. Wang, M. Mirza, Z. Wang, K. Xu, and J. He, Topological surface transport properties of single-crystalline SnTe nanowire, Nano Lett. **13**, 5344 (2013).

[17] A. A. Taskin, F. Yang, S. Sasaki, K. Segawa, and Y. Ando, Topological surface transport in epitaxial SnTe thin films grown on Bi_2Te_3, Phys. Rev. B **89**, 121302(R) (2014).

[18] B. A. Assaf, F. Katmis, P. Wei, B. Satpati, Z. Zhang, S. P. Bennett, V. G. Harris, J. S. Moodera, and D. Heiman, Topological surface transport in epitaxial SnTe thin films grown onBi_2Te_3, Appl. Phys. Lett. **105**, 102108 (2014).

[19] R. Akiyama, K. Fujisawa, T. Yamaguchi, R. Ishikawa, and S. Kuroda, Weak antilocalization in (111) thin films of a topological crystalline insulator SnTe, Nano Res. **9**, 490 (2016).

[20] B. A. Assaf, T. Phuphachong, V. V. Volobuev, A. Inhofer, G. Bauer, G. Springholz, L. A. de Vaulchier, and Y. Guldner, Massive and massless Dirac fermions in $Pb_{1-x}Sn_xTe$ topological crystalline insulator probed by magneto-optical absorption, Sci. Rep. **6**, 20323 (2016).

[21] T. Phuphachong, B. A. Assaf, V. V. Volobuev, G. Bauer, G. Springholz, L. A. de Vaulchier, and Y. Guldner, Dirac Landau level spectroscopy in $Pb_{1-x}Sn_xSe$ and $Pb_{1-x}Sn_xTe$across the topological phase transition: A review, Crystals **7**, 29 (2017).

[22] M. Liebmann *et al.*, Giant rashba-type spin splitting in ferroelectric GeTe(111), Adv. Mater. **28**, 560 (2016).

[23] J. Krempaský, H. Volfova, S. Muff, N. Pilet, G. Landolt, M. Radovic, M. Shi, D. Kriegner, V. Holy, J. Braun *et al.*, Disentangling bulk and surface Rashba effects in ferroelectric α-GeTe, Phys. Rev. B **94**, 205111 (2016).

[24] J. A. Sobota, S. Yang, J. G. Analytis, Y. L. Chen, I. R. Fisher, P. S. Kirchmann, and Z.-X. Shen, Ultrafast Optical Excitation of a Persistent Surface-State Population in the Topological Insulator Bi_2Se_3, Phys. Rev. Lett. **108**, 117403 (2012).

[25] J. A. Sobota, S.-L. Yanga, D. Leuenbergera, A. F. Kemper, J. G. Analytis, I. R. Fisher, P. S. Kirchmann, T. P. Devereaux, and Z.-X. Shen, Ultrafast electron dynamics in the topological insulator Bi_2Se_3 studied by time-resolved photoemission spectroscopy, J. Electron Spectrosc. Relat. Phenom. **195**, 249 (2014).

[26] Y. Ishida, T. Otsu, T. Shimada, M. Okawa, Y. Kobayashi, F. Iga, T. Takabatake, and S. Shin, Emergent photovoltage on SmB_6 surface upon bulk-gap evolution revealed by pump-and-probe photoemission spectroscopy, Sci. Rep. **5**, 8160 (2015).

[27] M. Neupane *et al.*, Gigantic Surface Lifetime of an Intrinsic Topological Insulator, Phys. Rev. Lett. **115**, 116801 (2015).

[28] J. Sánchez-Barriga, M. Battiato, E. Golias, A. Varykhalov, L. V. Yashina, O. Kornilov, and O. Rader, Laser-induced persistent photovoltage on the surface of a ternary topological insulator at room temperature, Appl. Phys. Lett. **110**, 141605 (2017).

[29] K. Sumida *et al.*, Prolonged duration of nonequilibrated dirac fermions in neutral topological insulators, Sci. Rep. **7**, 14080 (2017).

[30] Y. Ishida, T. Togashi, K. Yamamoto, M. Tanaka, T. Kiss, T. Otsu, Y. Kobayashi, and S. Shin, Time-resolved photoemission apparatus achieving sub-20-meV energy resolution and high stability, Rev. Sci. Instrum. **85**, 123904 (2014).

[31] R. Ishikawa, T. Yamaguchi, Y. Ohtaki, R. Akiyama, and S. Kuroda, Thin film growth of a topological crystal insulator SnTe on the CdTe (111) surface by molecular beam epitaxy, J. Cryst. Growth **453**, 124 (2016).

[32] See Supplemental Material at http://link.aps.org/supplemental/10.1103/PhysRevResearch.2.043120 for a movie file of the

TARPES images, movies of the temporal variation of ARPES images, the difference from that before the excitation, and the corresponding energy distribution curves (EDC).

[33] A. Nicolaou, V. Brouet, M. Zacchigna, I. Vobornik, A. Tejeda, A. Taleb-Ibrahimi, P. Le Fèvre, F. Bertran, S. Hébert, H. Muguerra, and D. Grebille, Experimental Study of the Incoherent Spectral Weight in the Photoemission Spectra of the Misfit Cobaltate $[Bi_2Ba_2O_4][CoO_2]_2$, Phys. Rev. Lett. **104**, 056403 (2010).

[34] S. Safaei, P. Kacman, and R. Buczko, Topological crystalline insulators (Pb,Sn)Te: Surface states and their spin polarization, Phys. Rev. B **88**, 045305 (2013).

[35] J. Liu, W. Duan, and L. Fu, Two types of surface states in topological crystalline insulators, Phys. Rev. B **88**, 241303(R) (2013).

[36] S. Zhu *et al.*, Ultrafast electron dynamics at the Dirac node of the topological insulator Sb_2Te_3, Sci. Rep. **5**, 13213 (2015).

[37] K. Ishizaka *et al.*, Giant Rashba-type spin splitting in bulk BiTeI, Nat. Mater. **10**, 521 (2011).

[38] E. Plekhanov, P. Barone, D. Di Sante, and S. Picozzi, Engineering relativistic effects in ferroelectric SnTe, Phys. Rev. B **90**, 161108(R) (2014).

[39] M. S. Bahramy *et al.*, Emergent quantum confinement at topological insulator surfaces, Nat. Commun. **3**, 1159 (2012).

[40] S. LaShell, B. A. McDougall, and E. Jensen, Spin Splitting of an Au(111) Surface State Band Observed with Angle Resolved Photoelectron Spectroscopy, Phys. Rev. Lett. **77**, 3419 (1996).

[41] M. Nagano, A. Kodama, T. Shishidou, and T. Oguchi, A first-principles study on the Rashba effect in surface systems, J. Phys. Condens. Matter **21**, 064239 (2009).

[42] J. Wang, J. Liu, Y. Xu, J. Wu, B.-L. Gu, and W. Duan, Structural stability and topological surface states of the SnTe (111) surface, Phys. Rev. B **89**, 125308 (2014).

[43] Y. Shi, M. Wu, F. Zhang, and J. Feng, (111) surface states of SnTe, Phys. Rev. B **90**, 235114 (2014).

Correction: Supplemental Material and the corresponding citation and description in Ref. [32] were not processed properly and have been set right.